Design of Inductive Power Transfer System With a Behavior of Voltage Source in Open-Loop Considering Wide Mutual Inductance Variation

Alberto Delgado, *Student Member, IEEE*, Nicolás Alonso Requena, *Student Member, IEEE*, Regina Ramos, *Student Member, IEEE*, Jesús Angel Oliver, *Member, IEEE*, Pedro Alou, *Member, IEEE*, and José Antonio Cobos, *Fellow, IEEE*

***Abstract*—This article analyses the fundamental aspects of the principal resonant network topologies for inductive power transfer systems. From the analytical derivation, different features, such as the variation of the coupling factor or load changes, are studied. Based on this study, a resonant series–series topology is selected, which cancels the leakage inductance. Due to the specifications, the air gap distance and its tolerance (±12%) produce a wide variation of the coupling factor of the inductive link. Therefore, through fast three-dimensional simulations by finite elements, the inductive link is designed so that this variation is minimized. This maintains the resonance and the designed system, in turn, behaves like a voltage source regardless of power, and thus, evades the implementation of a control stage. A dc–dc converter is constructed where the distance between the primary and secondary side vary from 35 to 45 mm, and the power ranges from 0 to 5 kW. The output voltage range goes from 38 to 55 V_{DC}. Experimental results for the dc–dc converter report an efficiency of over 94%.**

***Index Terms*—Inductive link, inductive power transfer (IPT) system, resonant converter, resonant network, wireless power transfer (WPT) system.**

I. Introduction

INDUCTIVE power transfer (IPT) systems is a continuously growing industry [1], thanks to its many benefits compared to electrical connection in some applications, e.g. the user does not need to interfere in the connection. Electric vehicles [2]–[7], battery charging for portable consumer electronics [8]–[10] and implantable devices [11]–[14] are an important focus of the IPT systems. In some of the abovementioned industrial applications, cost, maintenance, or even mechanical limitations make the use of physical connection a difficult task. Therefore, IPT systems represent a very important opportunity to solve these inconveniences.

Manuscript received January 20, 2020; accepted March 25, 2020. Date of publication April 12, 2020; date of current version July 20, 2020. This work was supported by the the Ministerio de Economia, Industria y Competitividad de España under Grants DPI2016-80953-R and RTC-2016-4820-4. Recommended for publication by Associate Editor O. C. Onar. *(Corresponding author: Alberto Delgado.)*

The authors are with the Centro de Electrónica Industrial, Universidad Politcnica de Madrid, 28602 Madrid, Spain (e-mail: a.delgado@upm.es; nicolas.alonso@upm.es; regina.ramos@upm.es; jesusangel.oliver@upm.es; pedro.alou@upm.es; ja.cobos@upm.es).

Color versions of one or more of the figures in this article are available online at http://ieeexplore.ieee.org.

Digital Object Identifier 10.1109/TPEL.2020.2984097

The common configuration of an IPT system can be shown in Fig. 1. The air-gap between the primary and the secondary inductor and its geometries will determine the self-inductance and the mutual inductance of the inductive link. Constant air-gap IPT converters and its control designs are widely studied in the literature [15]–[17]. IPT systems with variable air-gaps where the mutual inductance varies but self-inductances are practically constant are also well-known [2], [3], [10], [18]. Nevertheless, some applications have a wide air-gap variation between primary and secondary side which can change not only the mutual inductance but also the self-inductance. In this way, the tuning between transmitter/receiver and its resonant network may be misadjusted. If this happens, the resonant frequency and the operating point of the system will vary.

It can be solved using a frequency control that is extensively studied in the literature [2], [16]–[23].

For better understanding of the system design, this article examines three different resonant compensation topologies.

1) Typical series–series resonant compensation where the capacitors of the resonant network are tuned to the self-inductance of the coil [3], [4], [7], [8], [10].
2) Common series-parallel resonant compensation where the capacitors are tuned to part of the primary self-inductance of the coil and fully tuned to the secondary coil [5]–[7], [11], [13], [14].
3) Series-series resonant compensation where the capacitor cancels the leakage-inductance of both primary and secondary coils [24].

From these analyses, the three topologies are studied and the criterion for the selection of the resonant network that adapts to the specifications of the system is defined—power, transformation ratio of the voltage and current, the behavior of the system, the air-gap variation, etc.

Based on this analysis, the selected topology is series–series leakage resonant compensation. The tuning method of this topology depends on the leakage-inductance. It is this that depends on the coupling factor and the self-inductance.

This article focuses on the design of inductive links for series–series leakage resonant compensation to achieve constant leakage-inductance over the entire range of air-gap distances while maintaining high efficiency based on previous studies [25], [26]. Fast eddy current 3-D finite-element simulations are carried

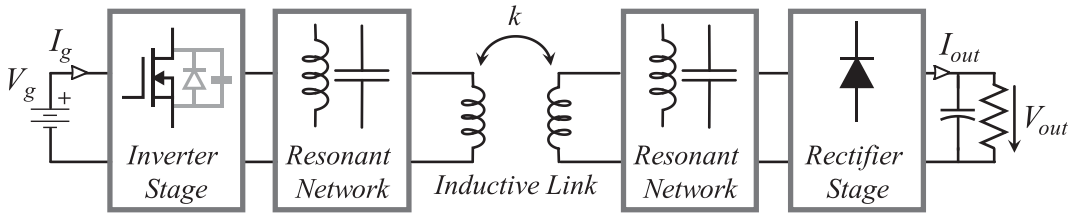

Fig. 1. Illustration of an inductive power transfer system—inverter stage, typically a full-bridge, primary resonant network based on capacitors and inductors, inductive coils, secondary resonant network (which can be different to the primary network), and a rectifier stage, typically diodes because it simplifies the control.

out using homogeneous models presented in previous work [25], [27]–[29] to allow simulations of inductive links with Litz-wire windings to be performed.

In this article, for the sake of clarity, the leakage inductance and the quality factor of an uncomplicated coil are obtained by conducting a set of finite-element parametric simulations. Later, electrical simulations of the inductive link are performed to evaluate whether the chosen topology can operate as a constant voltage source, independent of load, and air space variation.

Also, the design methodology presented in this study is validated using an IPT system designed for a large power range that goes from 0 kW (no load condition) up to 5 kW. The input voltage of the system will be 400 V_{DC}, the operating output voltage range goes from 38 to 55 V_{DC}.

This article is divided into five sections. Section II studies the fundamental analysis of an IPT system by deriving a simple electrical analysis. First, the first-harmonic approximation is used to simplify the analysis by modeling the inverter and the rectifier with an ac voltage source and equivalent resistor, respectively. Then, the inductive link is simplified by taking into account the resonant tank to simplify the analysis: 1) by using a T-model for series–series resonant network; b) by using a cantilever-model for series-parallel resonant network. Based on this approximation, conventional series–series resonant topology, basic series-parallel resonant topology, and series–series resonant topology where the capacitors are tuned with the leakage inductance are analyzed and described. Section III seeks to outline the problem statement dealt with in this article. Based on the specification of the system, one resonant compensation topology is selected. In Section IV, based on the previous fundamental analysis, a design criterion is found for the inductive links used in series–series leakage resonant compensation to mitigate the effects of the air-gap variation which will maintain the resonance of the system, and thus, allow the system to operate as a voltage source in open-loop. In Section V, the built prototype is described, and measurements and simulations are compared to validate the design criteria.

II. Fundamental Analysis of IPT System

Fig. 1 shows the typical architecture utilized in inductive power transmission. The inverter stage is habitually a full-bridge inverter, and the rectifier stage can be either a controlled full-bridge or a diode rectifier. In this article, the inverter stage is a full-bridge inverter, and the rectifier is a full-bridge diode rectifier.

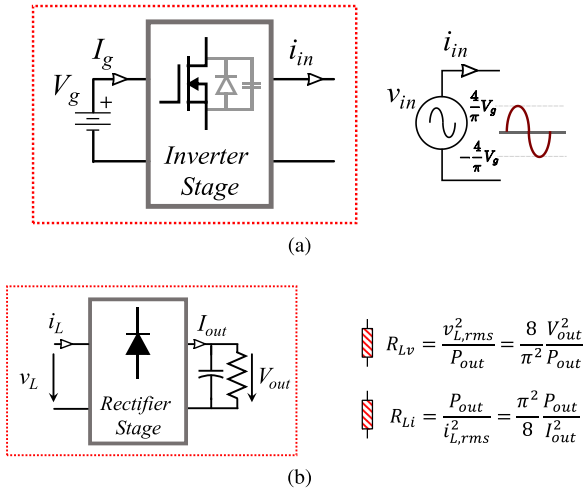

Fig. 2. (a) Equivalent ac input voltage source as presented by full-bridge MOSFET inverter stage. (b) Equivalent ac resistor as presented by full-bridge diode rectifier and load.

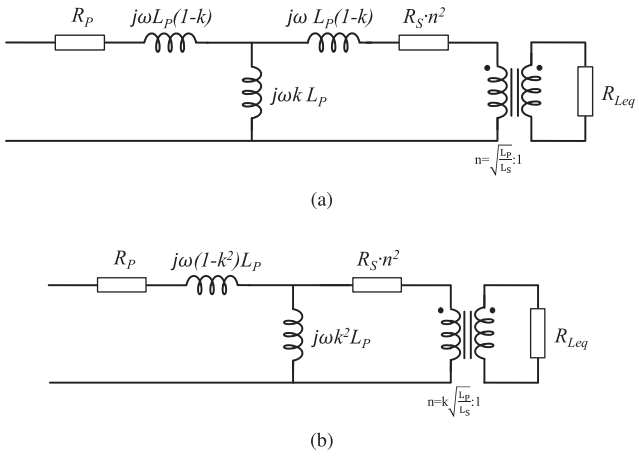

Fig. 3. Representation of the equivalent circuit model of an inductive link. (a) T-model representation. (b) Cantilever model representation.

The circuit is analyzed assuming the first harmonic approximation [15], [30]. It is reasonable to replace the inverter stage with an ac voltage source [see Fig. 2(a)]. The rectifier is substituted with its equivalent resistor, as shown in Fig. 2(b) [30]. The behavior of the circuit, as a current source or voltage source, determines the value of the equivalent resistor.

The inductive link showed in Fig. 1 can be modeled in different forms [31]–[34]: 1) T-model, as in Fig. 3(a); 2) cantilever model,

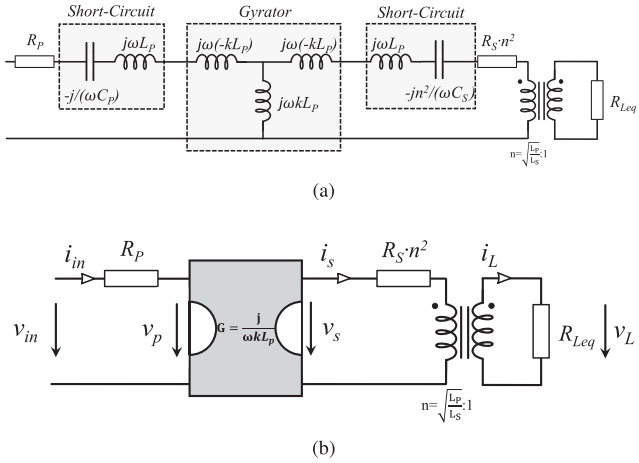

Fig. 4. Schematic representation of (a) IPT system with a series–series resonant network as current source. (b) Equivalent circuit of (a) when the resonance occurs.

as in Fig. 3(b), where L_p and L_s are the self-inductances of the primary and secondary side, respectively, k is the coupling factor, R_p and R_s are the self-resistances of the primary and secondary coil, respectively, and n is the ratio between primary and secondary side of the ideal transformer of each model.

For the sake of facilitating the analysis of the diverse topologies, we utilize the representation in T-model to analysis the series–series circuits, and the representation in the cantilever form is employed to study the series-parallel circuit.

In T-model, n is

$$n_T = \sqrt{\frac{L_p}{L_s}} \cong \frac{N_p}{N_s}. \tag{1}$$

And the relation n in the cantilever model is

$$n_C = k\sqrt{\frac{L_p}{L_s}} \tag{2}$$

A. Series–Series Resonant Compensation

This topology is based on series–series resonant network that consists of a resonant capacitor placed in series with the primary and the secondary inductor. Both resonant capacitors are tuned with the self-impedance of the inductive coils. The value of the capacitors at the switching angular frequency ω_s are

$$C_p = \frac{1}{\omega_s^2 L_p} \tag{3}$$

$$C_s = \frac{1}{\omega_s^2 L_s}. \tag{4}$$

Thus, the self-impedances L_p and $n^2 L_s$ with C_p and C_s/n^2, respectively, behave as a short circuit at the resonance frequency, as can be shown in Fig. 4(a). The result of this is a T circuit that has the gyrator's behavior [35] so that, essentially, the output current of the quadripole depends on the gyrator's forward gain G and the input voltage. The input current and output voltage have an analog relation. That is

$$\begin{aligned} I_s &= G \times V_p \\ I_{\text{in}} &= -G \times V_s \end{aligned} \tag{5}$$

where G is

$$G = \frac{1}{j\omega k L_p}. \tag{6}$$

Regarding Fig. 4(b), an abbreviated expression of the output current is readily derived using the gain of the gyrator as long as we depreciate the resistances (R_p and R_s) due to the nonideal inductors. By the application of the gyrator equation, it follows that the output current depends on the frequency, the coupling factor, and the inductance value

$$I_L = \frac{jV_{\text{in}}}{\omega n_T k L_s}. \tag{7}$$

Due to the fact that the output current depends on the input voltage, which is constant like the inductance value and the coupling factor, it is straightforward to deduce that (7) describes the behavior of a current source.

Moreover, from the expression (7), it is immediately noticed that for a coupling factor k and an angular switching frequency ω_s, the value for the secondary inductance needed to achieve the output current expected is

$$L_s = \frac{V_{\text{in}}}{\omega k n_T I_L}. \tag{8}$$

Consequently

$$L_p = \frac{n_T V_{\text{in}}}{\omega k I_L}. \tag{9}$$

Therefore, it is possible to calculate the power losses due to the ac resistances of the coils as

$$P_R = I_{\text{in}}^2 R_P + I_s^2 R_s n_T^2 = R_p(I_{\text{in}}^2 + I_s^2). \tag{10}$$

Using (5)

$$I_{\text{in}} = \frac{-jn_T V_L}{\omega k L_p}. \tag{11}$$

Also, the secondary current is

$$I_s = \frac{V_L}{n_T R_{Leq}}. \tag{12}$$

Simplifying the expression (10) using (9), (11), and (12), the maximum efficiency of the link is

$$\eta_{\text{link}} = 1 - \frac{2}{kQ}. \tag{13}$$

B. Series-Parallel Resonant Compensation

This topology is based on a series-parallel resonant network that is composed of a resonant capacitor placed in series with the primary inductor and a resonant capacitor set in parallel with the secondary inductor.

The primary resonant capacitor is tuned with the primary self-inductance multiplied by a factor of $(1 - k^2)$; the secondary resonant capacitor is tuned with the secondary self-inductance.

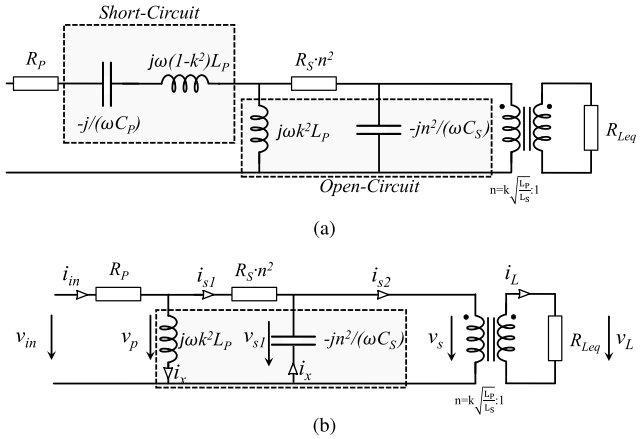

Fig. 5. Schematic representation of (a) IPT system with a series-parallel resonant network as voltage source. (b) Equivalent circuit of (a) when the resonance occurs.

By doing so, it is possible to achieve a constant voltage source independently of the load.

Thus, it is necessary to define the value of the primary and secondary capacitor at the switching angular frequency ω_s as

$$C_p = \frac{1}{\omega_s^2 L_p(1-k^2)} \tag{14}$$

$$C_s = \frac{1}{\omega_s^2 L_s}. \tag{15}$$

By doing so, the impedances $L_p(1-k^2)$ on the left side and $L_p k^2$ on the right side with C_p and C_s/n^2, respectively behave as a short circuit and open circuit, reciprocally, at the resonance frequency, as can be shown in Fig. 5(a).

In order to obtain the simplified expression of the output voltage, resistors due to the nonideal inductors are neglected [see Fig. 5(b)]. By the application of the Kirchhoff law, it follows that the output voltage depends on the input voltage, the inductive link turns-ratio and the nominal coupling factor

$$V_L = \frac{V_{\text{in}}}{n_C}. \tag{16}$$

From (16), it is easy to verify that the behavior of this resonant topology is merely a voltage source because the output voltage only depends on the input voltage and the turn ratio of this topology.

Analyzing the power losses due to the ac resistances of the coils, it is possible to obtain an expression to calculate the optimal values of L_p and L_s in order to minimize the losses in the system. Thus, calculating the power losses as

$$P_R = I_{in}^2 R_P + I_{S1}^2 R_s n_C^2 \tag{17}$$

where I_{in} and I_{s1} are rms values.

The secondary current I_{s2} can be calculated as

$$I_{s2} = \frac{V_L}{R_{Leq} n_C}. \tag{18}$$

Then, the input current is

$$I_{\text{in}} = I_{s2}. \tag{19}$$

The current through the parallel inductance can be expressed as

$$I_x = \frac{V_{\text{in}}}{j\omega k^2 L_p} = \frac{V_L}{j\frac{\omega k^2 L_p}{n_C}}. \tag{20}$$

Thus, the current I_{s1} can be expressed by using (18) and (20) as

$$I_{s1} = V_L \frac{\sqrt{\omega^2 k^4 L_p^2 + n_C^4 R_{Leq}^2}}{\omega k^2 L_p n_C R_{Leq}} \tag{21}$$

where V_L is the rms value.

Simplifying the expression (17) using (19) and (21) leads to

$$P_R = \frac{P_{\text{out}}}{Q}\left[\frac{\omega L_s}{R_{Leq}}\left(1+\frac{1}{k^2}\right)+\frac{R_{Leq}}{\omega L_s}\right]. \tag{22}$$

Then, the calculation of the optimum value of L_s that minimizes the losses is

$$\frac{dP_r}{dL_s} = 0 \longrightarrow L_s = \frac{kR_{L_{eq}}}{\omega_s\sqrt{k^2+1}}. \tag{23}$$

Consequently using (16)

$$L_p = L_s\left(\frac{V_{\text{in}}}{kV_L}\right)^2. \tag{24}$$

Thus, using this expression in (22) the maximum efficiency of the link is

$$\eta_{\text{link}} = 1 - \frac{2\sqrt{k^2+1}}{kQ}. \tag{25}$$

C. Series–Series Leakage Resonant Compensation

The series–series resonant network is founded on a resonant capacitor in series with the primary inductor; also, a resonant capacitor is situated in series with the secondary inductor. In order to achieve a constant voltage source in this configuration, where the output voltage does not depend on the power demanded (load-independent), it is essential to tune the primary and secondary capacitors with the impedance that is in series with them, the leakage inductance.

Then, it is crucial to define the value of the primary and secondary capacitor at the switching angular frequency ω_s as

$$C_p = \frac{1}{\omega_s^2 L_p(1-k)} \tag{26}$$

$$C_s = \frac{1}{\omega_s^2 L_s(1-k)}. \tag{27}$$

By doing so, the impedances $L_p(1-k)$ and $L_s(1-k)$, with C_p and C_s, respectively, work as a short circuit at the resonance frequency, as shown in Fig. 6(a).

With the aim of obtaining the simplified expression of the output voltage, resistors due to the nonideal inductors are neglected [see Fig. 6(b)]. By the application of the Kirchhoff law, it follows that the output voltage depends on the input voltage (it is a voltage source as the previous topology) and the inductive link turns-ratio

$$V_L = \frac{V_{\text{in}}}{n_T}. \tag{28}$$

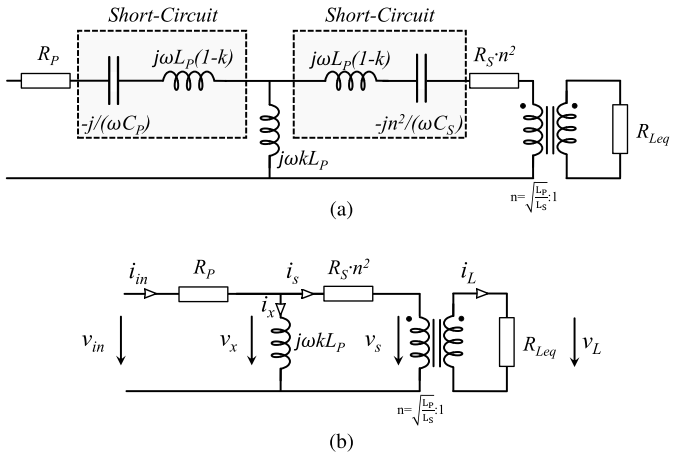

Fig. 6. Schematic representation of (a) IPT system with a series–series resonant network as voltage source. (b) Equivalent circuit of (a) when the resonance occurs.

Analyzing the power losses due to the ac resistances of the coils, it is possible to obtain an expression to calculate the optimal values of L_p and L_s in order to minimize the losses in the system. Thus, calculating the power losses as

$$P_R = I_1^2 R_p + I_2^2 R_s n_T^2 \tag{29}$$

where I_1 and I_2 are rms values. The primary current can be expressed then as

$$I_1 \cong V_{\text{in}} \frac{\sqrt{R_{L_{eq}}^2 n_T^4 + \omega^2 k^2 L_p^2}}{\omega k L_p R_{L_{eq}}}. \tag{30}$$

And the secondary current as

$$I_2 \cong \frac{V_{\text{in}}}{R_{L_{eq}} n_T^2} \tag{31}$$

where V_{in} is the rms value.

Simplifying the expression (29) using (30) and (31) leads to

$$P_R = V_L^2 \frac{\omega L_p}{Q} \left[\frac{R_{L_{eq}}^2 n_T^4 + 2\omega^2 L_p 2}{R_{L_{eq}}^2 n_T^2 \omega^2 L_p^2} \right]. \tag{32}$$

Then, the calculation of the optimum value of L_s that minimizes the losses is

$$\frac{dP_r}{dL_s} = 0 \longrightarrow L_s = \frac{R_{L_{eq}}}{\omega_s k \sqrt{2}}. \tag{33}$$

Consequently

$$L_p = L_s \left(\frac{V_{\text{in}}}{V_L} \right)^2. \tag{34}$$

Thus, using this expression in (29), the maximum efficiency of the link is

$$\eta_{\text{link}} = 1 - \frac{2\sqrt{2}}{kQ}. \tag{35}$$

TABLE I
SUMMARY OF THE RESONANT TOPOLOGIES

Topology	Efficiency	Behavior	Ls Current
SS	$1-\frac{2}{kQ}$=97.77%	Current Source	$111A_{rms}$
SP	$1-\frac{2\sqrt{k^2+1}}{kQ}$=97.67%	Voltage Source	$430A_{rms}$
SS-Lk	$1-\frac{2\sqrt{2}}{kQ}$=96.85%	Voltage Source	$111A_{rms}$

III. Problem Statement and Selection of a Compensation Method

The specification of the system is an IPT converter which operates with an input voltage of 400 V and an output voltage range from 38 to 55 V working from 0 up to 5 kW. The gap distance between the emitter and the receiver is 40 ± 5 mm.

Based on the previous mere mathematical derivations, the selection of resonant network compensation is explained in details from the standpoint of behavior (current or voltage source), efficiency, the air-gap variation, and the inductive link design (high current, voltage, etc.).

In order to establish a basis for comparing the resonant network analyzed in this article, a quality factor of 300 and a nominal coupling factor of $k = 0.3$ are considered.

The analysis of the resonant topologies starts with the comparison of the performances of the different inductive link according to the resonant network chosen. Series–series resonant compensation presents the highest efficiency. Series-parallel resonant compensation has 5% more losses than the first. The worst of these topologies is the series–series leakage-inductance resonant compensation, which has 40% more. In terms of performance, and using the same values of Q and k, the results show that the conventional SS resonant compensation presents 97.77% of efficiency, SP resonant compensation reports an efficiency of 97.67%, and SS leakage-inductance shows 96.85% of performance. Table I compiles the equation of the efficiency of each topology and the particular values for the considered coupling factor and quality factor.

The behavior of the SS resonant compensation, despite its superior efficiency, constitutes a challenge in ensuring that the output voltage in the required range. This is because this topology is a current source which means that the output current is constant and acts independently of the load. Since the output current is constant, the higher the load (the higher the power), the higher the output voltage must be. It is then possible to adjust the maximum voltage to meet the specifications. The problem occurs when the load tends to lower values, i.e., when the power is low (about 0 kW), the output voltage should decrease to 0 V. Then, the output voltage requirements are not met over the entire power range. Therefore, this topology is not adequate for this application.

The second most efficient topology is the one using SP resonance compensation. In contrast to SS resonant network, in SP, even if the load changes, the output voltage is constant. However, if the coupling factor changes due to the air-gap variations, the output voltage changes proportionally due to the turn-ratio of the system [it is defined by (2)]. Moreover, this topology needs an output inductor connected in series between the tank capacitor

and the power converter due to the parallel capacitor placed with the receiver.

Regarding coupling factor variations, and therefore output voltage fluctuations, due to the broad range of output voltage specified, it is possible to design the inductive link to reduce the variation of coupling factor, keeping the output voltage in range. By doing so, it is possible to eliminate the control loop and the wireless-communication latency problems. However, due to the fact that the control is eliminated, the ratio between the transmitter and receiver must be adapted to obtain a voltage ratio of 8.

The optimum value for the secondary inductor for this application should be 185 nH. Then if a voltage drop of 45 V_{rms} occurs in the receiver, the circulating current through the inductor is 430 A_{rms}. This fact means that the amount of copper required to achieve a reasonable current density is considerable. For this reason, this topology is not very appropriate when the ratio between primary and secondary are large.

Even though SS leakage-inductance resonant compensation is the most critical from an efficiency point of view, it presents the most desirable characteristics from the behavior standpoint. Analogous to SP, this topology serves as a voltage source. Furthermore, the output voltage does not depend on the coupling factor if the resonance is kept. Additionally, the current through the receiver is the same as the output current of the system—111 A_{rms}.

In light of the above, the series–series leakage-inductance resonant compensation is chosen, where a design criterion for the inductive link is described and discussed in the following section.

Table I summarizes the characteristics of each circuit described in this section.

IV. Design Criterion for SS Leakage-Inductance Resonance to Operate in Open-Loop

From C_p and C_s tuning method (26) and (27), it is trivial to deduce that the resonance depends on the self-inductance and the coupling factor, i.e., on the leakage-inductance. Assuming that primary and secondary coils are identical, the inductive link at the nominal distance has a self-inductance L_0 and a coupling factor k_0. Considering a variation in the distance, the self-inductance changes to L_1 and the coupling factor to k_1. In this article, instead of using a control stage to change the frequency in order to keep the output voltage in range, a design criterion to maintain the leakage inductance, and then the resonant condition in the inductive link even if the air gap varies is proposed. It is defined as

$$(1-k_0)L_0 = (1-k_1)L_1. \tag{36}$$

In (36), it is easy to notice that the leakage-inductance must be constant over the whole range of air gap distances. By defining $L_1 = \alpha_L L_0$ and $k_1 = \alpha_k k_0$, the following expression is derived:

$$\alpha_k = \frac{\alpha_L + (k_0 - 1)}{k_0 \alpha_L} \tag{37}$$

where α_L and α_k represent the variation of L_0 and k_0, respectively. If the variation of the self-inductance and coupling factor is irremediably in the required range of air gap, taking the criterion of (37), the same resonant frequency is kept, obtaining the voltage gain showed in Fig. 7. In this voltage gain, it is noticed that in the nominal frequency for each distance, there is unity gain.

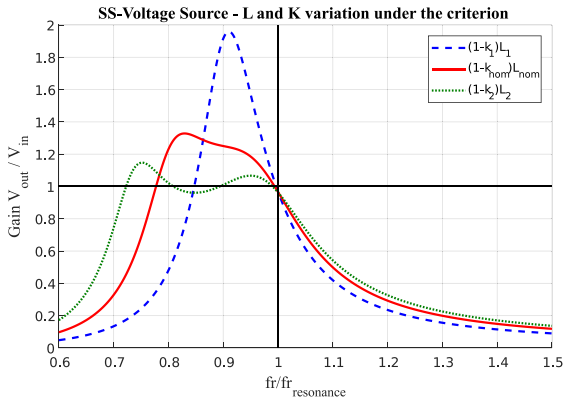

Fig. 7. Simulated bode results of a inductive link that consists of a primary and secondary coil with a self-inductance of 115 μH and a coupling factor of 0.25 when the self-inductance and the coupling factor change following the criterion (37).

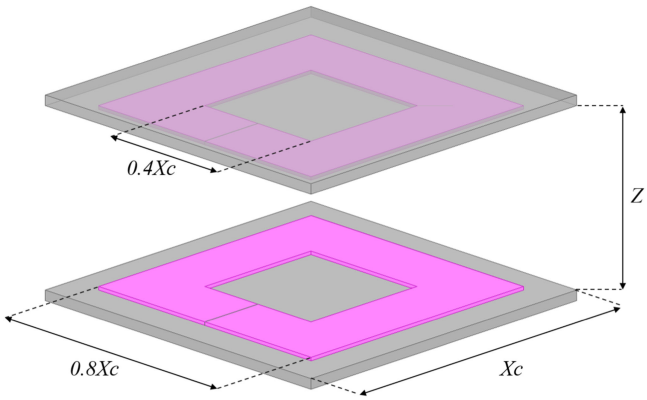

Fig. 8. Geometry and parameters of the finite-element model built in Ansys Maxwell.

However, this is an ideal case. In a practical case, if the design of the inductive link tries to follow the criterion, there are slight variations in the leakage inductance that modifies the output voltage value.

Fig. 8 shows the considered model for the inductive link which has two degrees of freedom—Xc and Z. The winding dimension is proportional to the core dimension in order to simplify the practical case.

In order to quantify these output voltage variations, a set of magnetostatic 3-D simulations using a finite-element tool, as Ansys Maxwell, in combination with the models presented in [25], [27]–[29] are performed. The parameter Xc is set to vary from 50 to 300 mm. Also, the air gap distance is set to vary from 20 to 60 mm. From the design space mentioned above, the inductance and coupling factor (then the leakage inductance) of the simulated coil are obtained.

Fig. 9(a) shows the leakage inductance for each value of Xc and for the Z range from 30 to 50 mm. The black vertical lines limit the air-gap range analyzed. The horizontal black lines limit the maximum leakage inductance variation allowed for

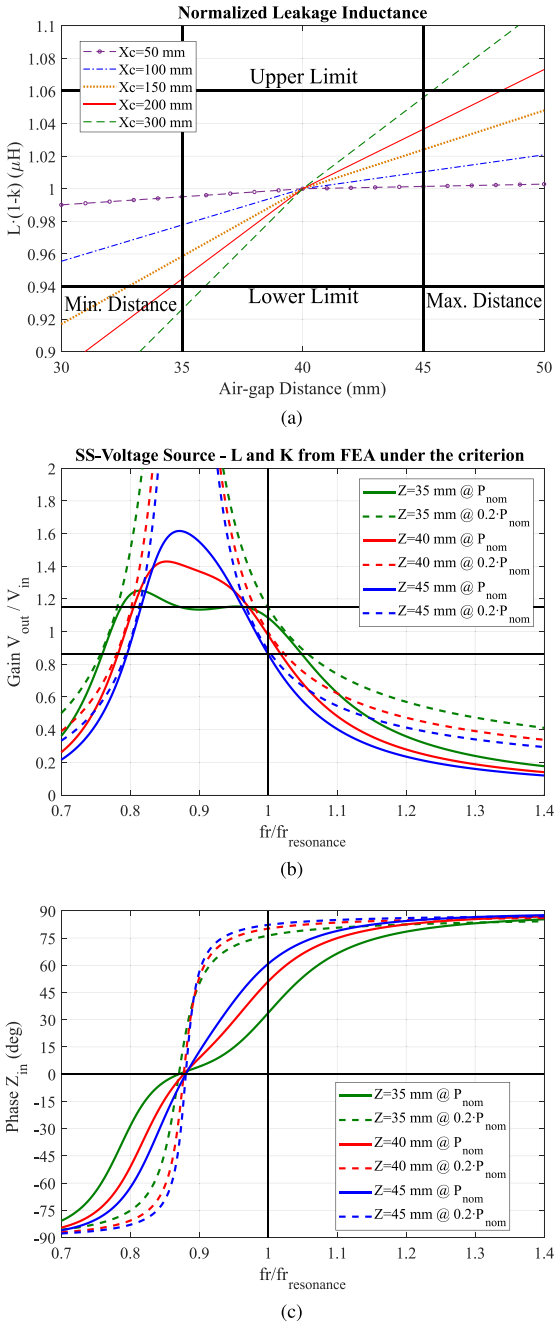

Fig. 9. Results of the FEA model. (a) Leakage inductance finite-element results for different Xc values. (b) Gain voltage of the system when the self-inductance and the coupling factor change trying following the criterion (37). (c) Phase-angle of the input impedance of the system when the self-inductance and the coupling factor change trying following the criterion (37).

the nominal output voltage of 46.5 V_{DC} to be in range for this particular application.

Analyzing the leakage inductance normalized to the nominal case Z = 40 mm, the smaller the coil size is, the more constant the leakage inductance is in the analyzed Z range. Nevertheless, smaller coils in this air-gap distance also means smaller coupling factor and lower efficiency.

For this reason, in order to obtain the maximum performance complying with the limits presented in Fig. 9(a), the giant inductive coil that fits in the available area of the specifications

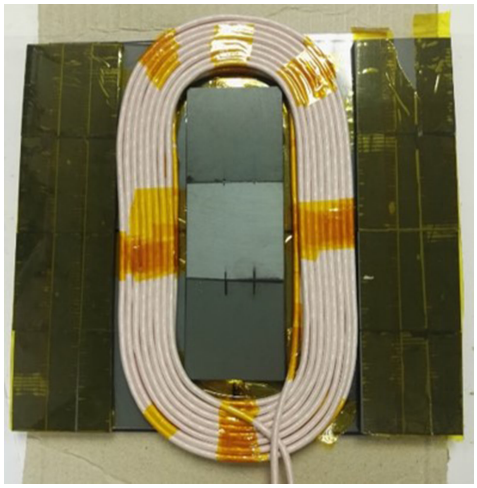

Fig. 10. Photograph of the primary IPT coil with a winding made from litz wire with 630 strands of 0.1-mm diameter.

is selected. Then, from the air gap being 40 ± 5 mm (±12%), the normalized leakage inductance to the nominal case is [0.95, 1, 1.04].

Following the proposed design criteria, the voltage gain has smaller variations [see Fig. 9(b)]. By keeping the nominal output voltage (46.5 V_{DC}), the output voltage at the maximum air-gap distance is 40 V_{DC}, and the minimum air-gap is 50.2 V_{DC}.

In this resonance mode, it can be seen that regardless of the power demand and the distance between coils, there is always a positive phase [see Fig. 9(c)]. This fact guarantees that ZVS can be obtained, thus reducing the losses of the inverter stage.

V. Experimental Results

A prototype is built to verify the theoretical analysis.

The inverter employed in this prototype is made of two evaluation boards designed by CREE (each evaluation board is a half-bridge module KIT8020CRD8FF1217P-1). The switches mounted on the evaluation boards modules are SiC MOSFETs from CREE model C2M0025120D. The diodes are C4D20120D since they only need to conduct during the dead-times of the inverter. The primary resonant capacitor is formed by three capacitors in parallel and six in series to get a final value of 34 nF using 2 kV 68 nF B32654 capacitors from TDK.

The coils have been manufactured using ferroxcube 3C95 ferrite tiles. The size is 200 mm × 200 mm. The geometry is similar to that of E-Cores (see Fig. 10). The litz wire consists of 630 strands of 0.1-mm diameter following the design guidelines of [26]. The primary inductive link has 16 turns in series; the secondary has 2 turns in series and 8 in parallel due to the high current. Results of finite-element analysis (FEA) and measurement (MEA) for the primary and secondary inductances, as well as the coupling factor, are presented in Table II. FEA and MEA exhibit good matching in all the cases.

For the receiver, the resonant capacitor has 27 parallel capacitors 1.6 kV 68 nF B32654 from TDK to obtain 1.8 μF of capacitance. The rectifier is made of 160 A 100 V STPS160H100TV diodes from STMicroelectronics. Finally, the output capacitance is made of 30 capacitors of 3.3 μF and 250 V from TDK, model B32654.

TABLE II
INDUCTIVE LINK SPECIFICATIONS

Distance (mm)		L_p (μH)	L_s (μH)	k (%)	$\frac{L_{Lp}}{L_{Lpnom}}$	$\frac{L_{Ls}}{L_{Lsnom}}$
35	*FEA*	117	2	37		
	MEA	119	2.18	35	0.983	0.965
40	*FEA*	113	1.9	32		
	MEA	114	2.14	31	1	1
45	*FEA*	111	1.9	28		
	MEA	113	2.12	26	1.063	1.068

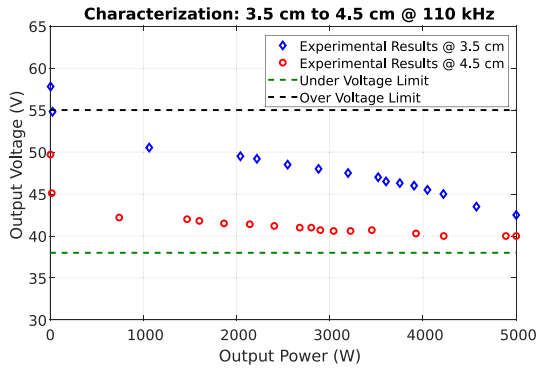

Fig. 11. Measurement results of the dc–dc converter when the output power is varied. (a) Output voltage. (b) Efficiency of the IPT system.

The output voltage and efficiency results along the whole power range are presented in Fig. 11. From 1 kW on, the output voltage at the two extreme gap distances are within the limits and with high efficiencies (more than 90%). At no load and 45 mm of gap distance, the voltage goes beyond the limits. This is the reason why a dummy load of 50 W is added, leading to a maximum output voltage of 55 V.

Fig. 12 shows the capture of the oscilloscope at 5 kW and the lowest distance (35 mm). The measures presented are the gate-source voltage and drain-source voltage of an inverter MOSFET, the primary current and the input current when the input voltage is 400 V. Due to the parasitics of the converter, we have adjusted the switching frequency to 110 kHz to reach the desired output voltage value along the Z-range air gap. The current shows an inductive behavior, helping to achieve ZVS, as no overshoot in the drain-source voltage is presented.

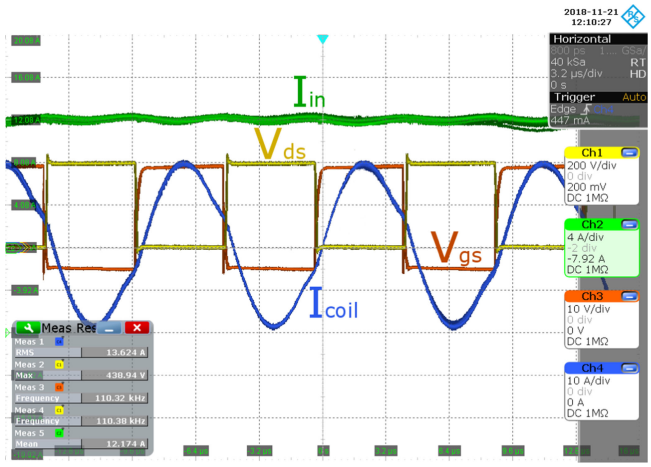

Fig. 12. Measured waveforms of the dc–dc converter for an air-gap of 3.5 cm at nominal power. The green waveform is the input dc current of the system, the blue waveform is the resonant ac current of the primary coil, the yellow waveform is the drain-source of one low-side MOSFET of the inverter, and the orange waveform is the grate-source of the same MOSFET.

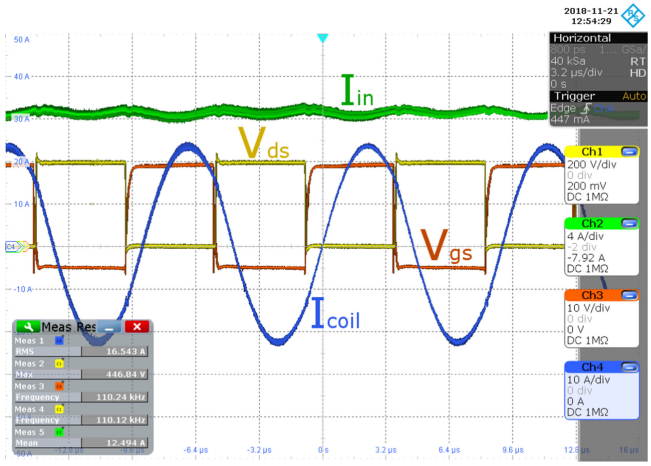

Fig. 13. Measured waveforms of the dc–dc converter for an air-gap of 4.5 cm at nominal power. The green waveform is the input dc current of the system, the blue waveform is the resonant ac current of the primary coil, the yellow waveform is the drain-source of one low-side MOSFET of the inverter, and the orange waveform is the grate-source of the same MOSFET.

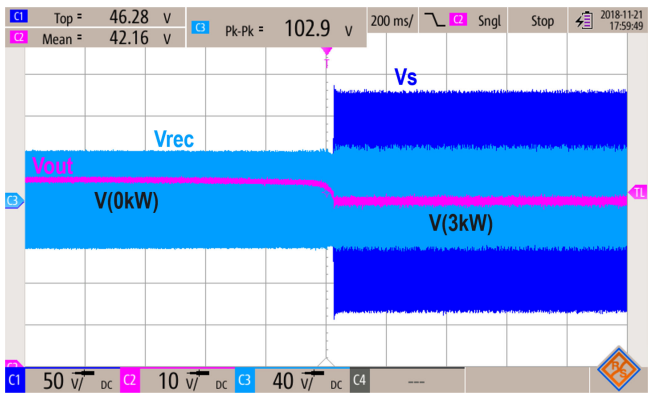

Fig. 14. Waveforms measured during power step from 0 to 3 kW. The pink waveform is the output voltage, the light blue waveform is the rectifier voltage, and the dark blue waveform is the voltage of the secondary coil.

Fig. 13 also shows the same waveforms at the 5-kW point, but at the highest distance (45 mm). An interesting finding is the higher phase in current, going from 13.6 A in the previous case to 16.5 A; although, it still presents inductive behavior. A particular point to be highlighted is since the air-gap distance increases, the magnetizing inductance decreases [see Fig. 6(b)]. Due to that fact, the system consumes a higher reactive power, in turn, increasing the phase angle of the input impedance. For this reason, the current peak in the farthest position is higher.

Fig. 14 shows a power step from 0 to 3 kW, where it is possible to notice that the output voltage is kept in the range by the application without control.

VI. Conclusion

This article analyses three different resonant network topologies by means of simple analytical equations based on simplifications.

Analyzing losses, behavior of the converter (as voltage source or current source), air-gap variation effects, load dependencies, and current through the inductors, one of the topology is selected to meet with the application's specifications.

The resonant compensation topology selected is series–series where the capacitors are tuned with the leakage-inductance. From this, it is possible to achieve a constant voltage regardless of load and coupling factor as long as the resonance is maintained. To meet this, along with the air-gap range, constant leakage-inductance must be achieved.

For this purpose, fast eddy current 3-D finite-element simulations are carried out to obtain a design of an inductive coil that agrees with the design criterion developed in this article. With this design, it is plausible to obtain an almost constant leakage-inductance, keeping the resonance frequency and the behavior of voltage source.

In order to validate the methodology described in this article, an IPT system is simulated and built. From the simulation and the experimental results, it is noticed that the converter can operate in open-loop keeping the output voltage within the range. Due to the inductive behavior of the system, it is possible to achieve the ZVS condition. The efficiency of the system is kept over 94% throughout the entire range of operation.

Acknowledgment

The authors would like to thank UTRC for the support regarding many aspects of this article.

References

[1] G. A. Covic and J. T. Boys, "Inductive power transfer," *Proc. IEEE*, vol. 101, no. 6, pp. 1276–1289, Jun. 2013.

[2] M. Kim, D. Joo, and B. K. Lee, "Design and control of inductive power transfer system for electric vehicles considering wide variation of output voltage and coupling coefficient," *IEEE Trans. Power Electron.*, vol. 34, no. 2, pp. 1197–1208, Feb. 2019.

[3] C. Chen *et al.*, "Modeling and decoupled control of inductive power transfer to implement constant current/voltage charging and ZVS operating for electric vehicles," *IEEE Access*, vol. 6, pp. 59917–59928, 2018.

[4] O. C. Onar, M. Chinthavali, S. L. Campbell, L. E. Seiber, C. P. White, and V. P. Galigekere, "Modeling, simulation, and experimental verification of a 20-kw series-series wireless power transfer system for a Toyota RAV4 electric vehicle," in *Proc. IEEE Transp. Electrific. Conf. Expo.*, Jun. 2018, pp. 874–880.

[5] R. Bosshard, J. W. Kolar, J. Mhlethaler, I. Stevanovi, B. Wunsch, and F. Canales, "Modeling and η-α-Pareto optimization of inductive power transfer coils for electric vehicles," *IEEE J. Emerg. Sel. Topics Power Electron.*, vol. 3, no. 1, pp. 50–64, Mar. 2015.

[6] R. Bosshard, U. Badstbner, J. W. Kolar, and I. Stevanovi, "Comparative evaluation of control methods for inductive power transfer," in *Proc. Int. Conf. Renewable Energy Res. Appl.*, Nov. 2012, pp. 1–6.

[7] C.-S. Wang, O. H. Stielau, and G. A. Covic, "Design considerations for a contactless electric vehicle battery charger," *IEEE Trans. Ind. Electron.*, vol. 52, no. 5, pp. 1308–1314, Oct. 2005.

[8] A. P. Sample, D. T. Meyer, and J. R. Smith, "Analysis, experimental results, and range adaptation of magnetically coupled resonators for wireless power transfer," *IEEE Trans. Ind. Electron.*, vol. 58, no. 2, pp. 544–554, Feb. 2011.

[9] P. E. Jacobs, M. A. Kirby, E. T. Ozaki, and M. J. Mangan, "Wireless power transfer for chargeable devices," U.S. Patent Appl. 12/604223, Sep. 9, 2010.

[10] J. Yin, D. Lin, C. K. Lee, T. Parisini, and S. Y. . Hui, "Front-end monitoring of multiple loads in wireless power transfer systems without wireless communication systems," *IEEE Trans. Power Electron.*, vol. 31, no. 3, pp. 2510–2517, Mar. 2016.

[11] P. Si, A. P. Hu, S. Malpas, and D. Budgett, "A frequency control method for regulating wireless power to implantable devices," *IEEE Trans. Biomed. Circuits Syst.*, vol. 2, no. 1, pp. 22–29, Mar. 2008.

[12] M. P. Kesler *et al.*, "Wireless energy transfer for implantable devices," U.S. Patent 9577436, Feb. 21, 2017.

[13] X. Li, C. Tsui, and W. Ki, "A 13.56 MHZ wireless power transfer system with reconfigurable resonant regulating rectifier and wireless power control for implantable medical devices," *IEEE J. Solid-State Circuits*, vol. 50, no. 4, pp. 978–989, Apr. 2015.

[14] U. Jow and M. Ghovanloo, "Design and optimization of printed spiral coils for efficient transcutaneous inductive power transmission," *IEEE Trans. Biomed. Circuits Syst.*, vol. 1, no. 3, pp. 193–202, Sep. 2007.

[15] A. Berger, M. Agostinelli, S. Vesti, J. A. Oliver, J. A. Cobos, and M. Huemer, "A wireless charging system applying phase-shift and amplitude control to maximize efficiency and extractable power," *IEEE Trans. Power Electron.*, vol. 30, no. 11, pp. 6338–6348, Nov. 2015.

[16] J. P. Chow, H. Chung, C. Cheng, and W. Wang, "Use of transmitter-side electrical information to estimate system parameters of wireless inductive links," *IEEE Trans. Power Electron.*, vol. 32, no. 9, pp. 7169–7186, Sep. 2017.

[17] Z. Wang, Y. Li, Y. Sun, C. Tang, and X. Lv, "Load detection model of voltage-fed inductive power transfer system," *IEEE Trans. Power Electron.*, vol. 28, no. 11, pp. 5233–5243, Nov. 2013.

[18] Y. Su, H. Zhang, Z. Wang, A. P. Hu, L. Chen, and Y. Sun, "Steady-state load identification method of inductive power transfer system based on switching capacitors," *IEEE Trans. Power Electron.*, vol. 30, no. 11, pp. 6349–6355, Nov. 2015.

[19] R. Bosshard, J. W. Kolar, and B. Wunsch, "Control method for inductive power transfer with high partial-load efficiency and resonance tracking," in *Proc. Int. Power Electron. Conf.*, May 2014, pp. 2167–2174.

[20] U. K. Madawala, M. Neath, and D. J. Thrimawithana, "A power frequency controller for bidirectional inductive power transfer systems," *IEEE Trans. Ind. Electron.*, vol. 60, no. 1, pp. 310–317, Jan. 2013.

[21] J. Yin, D. Lin, C. Lee, and S. Y. R. Hui, "A systematic approach for load monitoring and power control in wireless power transfer systems without any direct output measurement," *IEEE Trans. Power Electron.*, vol. 30, no. 3, pp. 1657–1667, Mar. 2015.

[22] U. K. Madawala and D. J. Thrimawithana, "New technique for inductive power transfer using a single controller," *IET Power Electron.*, vol. 5, no. 2, pp. 248–256, Feb. 2012.

[23] X. Dai, Y. Sun, C. Tang, Z. Wang, Y. Su, and Y. Li, "Dynamic parameters identification method for inductively coupled power transfer system," in *Proc. IEEE Int. Conf. Sustain. Energy Technol.*, Dec. 2010, pp. 1–5.

[24] G. B. Joung and B. H. Cho, "An energy transmission system for an artificial heart using leakage inductance compensation of transcutaneous transformer," in *Proc. 27th Annu. IEEE Power Electron. Specialists Conf.*, Jun. 1996, vol. 1, pp. 898–904.

[25] A. Delgado, J. A. Oliver, J. A. Cobos, J. Rodriguez, and A. Jimnez, "Optimized design for wireless coil for electric vehicles based on the use of magnetic nano-articles," in *Proc. IEEE Appl. Power Electron. Conf. Expo.*, Mar. 2019, pp. 1515–1520.

[26] A. Delgado, D. Schoenberger, J. A. Oliver, P. Alou, and J. A. Cobos, "Design guidelines of inductive coils using a polymer bonded magnetic composite for inductive power transfer systems in electric vehicles," *IEEE Trans. Power Electron.*, to be published.

[27] A. Delgado, G. Salinas, J. A. Oliver, J. A. Cobos, J. Rodrguez, and S. L. Premo, "Equivalent parameters of round and litz wire conductors to obtain an equivalent layer to accelerate finite element simulations of wireless power transfer system," in *Proc. IEEE Energy Convers. Congr. Expo.*, Sep. 2018, pp. 7375–7379.
[28] A. Delgado, G. Salinas, J. Rodrguez, J. A. Oliver, and J. A. Cobos, "Finite element modelling of litz wire conductors and compound magnetic materials based on magnetic nano-particles by means of equivalent homogeneous materials for wireless power transfer system," in *Proc. IEEE 19th Workshop Control Model. Power Electron.*, Jun. 2018, pp. 1–5.
[29] A. Delgado, G. Salinas, J. A. Oliver, J. A. Cobos, and J. Rodriguez-Moreno, "Equivalent conductor layer for fast 3-D finite element simulations of inductive power transfer coils," *IEEE Trans. Power Electron.*, vol. 35, no. 6, pp. 6221–6230, Jun. 2020.
[30] R. L. Steigerwald, "A comparison of half-bridge resonant converter topologies," *IEEE Trans. Power Electron.*, vol. 3, no. 2, pp. 174–182, Apr. 1988.
[31] A. E. Fitzgerald, C. Kingsley, S. D. Umans, and B. James, *Electric machinery*, vol. 5. New York, NY, USA: McGraw-Hill, 2003.
[32] R. W. Erickson and D. Maksimovic, "A multiple-winding magnetics model having directly measurable parameters," in *Proc. 29th Annu. IEEE Power Electron. Specialists Conf. (Cat. No. 98CH36196)*, May 1998, vol. 2, pp. 1472–1478.
[33] D. Maksimovic, R. W. Erickson, and C. Griesbach, "Modeling of cross-regulation in converters containing coupled inductors," *IEEE Trans. Power Electron.*, vol. 15, no. 4, pp. 607–615, Jul. 2000.
[34] K. D. T. Ngo, S. Srinivas, and P. Nakmahachalasint, "Broadband extended cantilever model for magnetic component windings," *IEEE Trans. Power Electron.*, vol. 16, no. 4, pp. 551–557, Jul. 2001.
[35] Y. H. Sohn, B. H. Choi, G. Cho, and C. T. Rim, "Gyrator-based analysis of resonant circuits in inductive power transfer systems," *IEEE Trans. Power Electron.*, vol. 31, no. 10, pp. 6824–6843, Oct. 2016.

Alberto Delgado (Student Member, IEEE) received the B.Sc. degree in electrical engineering from the University of Málaga (UMA), Malaga, Spain, in 2016, and the M.Sc. degree in industrial electronics in 2017 from the Universidad Politécnica de Madrid (UPM), Madrid, Spain, where he is currently working toward the Ph.D. degree in industrial electronics.

He became a Teaching Assistant with UPM in 2019. His research interests include modeling of dc–dc converters for inductive power transfer system, magnetic components for different applications, such as RFID communications and wireless charging, and magnetic nano-materials and micro-materials.

Mr. Delgado was awarded honors on several occasions during his undergraduate studies and he was the recipient of the Best Student of the Year Award.

Nicolás Alonso Requena (Student Member, IEEE) was born in Madrid, Spain. He received the B.Sc. degree in industrial engineering (electrical option) and the M.Sc. degree in industrial engineering from the Universidad Politécnica de Madrid (UPM), Madrid, Spain in 2015 and 2018, respectively.

He is currently a Research Engineer in power electronics with UPM in projects related with dc/dc converters, three phase rectifiers, and wireless power transfer systems.

Regina Ramos (Student Member, IEEE) received the B.Sc. degree in electrical engineering in 2014, and the M.Sc. degree in industrial electronics in 2016 from the Universidad Politécnica de Madrid (UPM), Madrid, Spain, where she is currently working toward the Ph.D. degree in industrial electronics.

Her research interests include switching-mode power supplies, power architectures, and digital control applied to power electronics.

Jesús Ángel Oliver (Member, IEEE) received the master's and doctoral degrees in electrical engineering from the Universidad Politécnica de Madrid (UPM), Madrid, Spain, in 1996 and 2007, respectively.

In 2001, he became an Assistant Professor with UPM, where he became an Associate Professor in 2007. He has authored and coauthored more than 150 scientific papers in journals and conferences and holds five patents. His research interests include modeling (dc–dc converters, magnetic components, piezoelectric transformers, fuel-cells, and dc distributed power electronic systems), fast control techniques for dc–dc converters for VRM applications and RF amplifiers, three-phase rectifiers for aircraft applications, wireless power transfer, and power systems on chip.

Dr. Oliver has led numerous research projects with private and public funding and has participated in more than 50 direct R&D projects with companies in Europe, USA, Australia, and China. Currently, he is serving as an Associate Editor for the IEEE TRANSACTIONS ON POWER ELECTRONICS.

Pedro Alou (Member, IEEE) was born in Madrid, Spain, in 1970. He received the M.S. and Ph.D. degrees in electrical engineering from the Universidad Politécnica de Madrid (UPM), Madrid, Spain, in 1995 and 2004, respectively.

He has been involved in power electronics since 1995, participating in more than 50 R&D projects with the industry. He has authored or coauthored over 100 technical papers and holds five patents. He is currently an Associate Professor with UPM. His research interests include power supply systems, advanced topologies for efficient energy conversion, modeling of power electronics, advanced control techniques for high dynamic response, energy management and new semiconductor technologies for power electronics. His research activity is distributed among industrial, aerospace, and military projects.

José Antonio Cobos (Senior Member, IEEE) received the master's and doctoral degrees in electrical engineering from the Technical University of Madrid (UPM), Madrid, Spain, in 1989 and 1994, respectively.

He was the Founder Director with the Centro de Electrnica Industrial, Universidad Politécnica de Madrid (UPM), Madrid, Spain, (CEI-UPM), a university research center leading a strong industrial program in power electronics and digital systems, in 2006. Since 2016, he has been the Founder President of its Industrial Council, to coordinate education and research with industry. He is currently a Full Professor with UPM. His contributions are focused on power supply systems for industrial, aerospace, telecom, automotive, renewable energy, and medical applications. He advised over 50 graduate students, has authored or coauthored over 300 technical papers ($>$8000 citations, h $=$ 47), and is the co-inventor of patents with six companies. His current research interests include energy efficiency in digital systems, RF amplifiers, renewable energy, magnetic components, transcutaneous energy transfer, and biomedical applications.

Dr. Cobos was an Adcom Member of the Power Electronics Society (IEEE-PELS) and the Chair of its Technical Committee on dc power supply systems. He was the General Chair of PwrSoC 2016 (IEEE-PELS and Power Supply Manufacturers Association, PSMA) and an Associate Editor for the IEEE TRANSACTIONS ON POWER ELECTRONICS and the *PELS Letters*. He conducted professional seminars and tutorials in the USA, U.K., Austria, Germany, Italy, Sweden, Switzerland, Syria, Mexico, and Macedonia. He is a Steering Committee Member (Program Chair in 2019) of the IEEE Applied Power Electronics Conference (APEC). From 2016 to 2017, he was an RCC Fellow with Harvard University, Cambridge, MA, USA, and a Fulbrighter with the University of California at Berkeley, Berkeley, CA, USA.